Gravity Field of the Moon from the Gravity Recovery and Interior Laboratory (GRAIL) Mission

Maria T. Zuber[1]*, David E. Smith[1], Michael M. Watkins[2], Sami W. Asmar[2], Alexander S. Konopliv[2], Frank G. Lemoine[3], H. Jay Melosh[4], Gregory A. Neumann[3], Roger J. Phillips[5], Sean C. Solomon[6,7], Mark A. Wieczorek[8], James G. Williams[2], Sander J. Goossens[9], Gerhard Kruizinga[2], Erwan Mazarico[1], Ryan S. Park[2] and Dah-Ning Yuan[2]

Submitted to: *Science*
12 October 2012

Spacecraft-to-spacecraft tracking observations from the Gravity Recovery and Interior Laboratory (GRAIL) have been used to construct a gravitational field of the Moon to spherical harmonic degree and order 420. The GRAIL field reveals features not previously resolved, including tectonic structures, volcanic landforms, basin rings, crater central peaks, and numerous simple craters. From degrees 80 through 300, over 98% of the gravitational signature is associated with topography, which reflects the preservation of craters in highly fractured crust. The remaining 2% represents fine details of subsurface structure not previously resolved. Ghost craters in the maria are not abundant, consistent with underlying highland crust being significantly modified by dikes and intrusions. GRAIL elucidates the role of impact bombardment in homogenizing the distribution of shallow density anomalies on terrestrial planetary bodies.

The Moon is a key to deciphering the evolutionary history of the terrestrial planets because it is the most accessible planetary body that preserves a surface record spanning most of solar system history. Reconstructing planetary evolution requires an understanding of the structure of the interior, which contains information on bulk composition, differentiation, and the nature of heat generation and heat loss that has influenced the style, extent, and duration of volcanism and tectonics. The Gravity Recovery and Interior Laboratory (GRAIL) mission (*1*) was undertaken to map the lunar gravity field from crust to core to address, in the context of other remote sensing and *in situ* observations, fundamental questions in lunar evolution.

Aside from the influence of the Moon's gravity throughout Earth history in producing oceanic tides, lunar gravity has been an observation of interest since the earliest satellites

orbited the Moon and revealed the presence of mass concentrations or "mascons" associated with the large nearside impact basins (*2*). The Moon's synchronous rotation, which causes the same hemisphere always to face Earth, poses a special challenge in measuring gravity. The most common method entails measuring the frequency shift of the spacecraft radio signal from a tracking station on Earth, but this cannot be done on the Moon's farside. One approach to measuring farside gravity is through the use of a relay satellite, as was done by the recent Kaguya mission (*3*). Current spherical harmonic (*4*) lunar gravity models derived from tracking the Lunar Prospector and earlier orbiters (*5-7*) and from the more recent Kaguya orbiter (*3*) range from degree and order 100 to 150, providing an effective blocksize resolution of 54 to 36 km, respectively.

GRAIL is a spacecraft-to-spacecraft tracking mission at the Moon developed with heritage from the Gravity Recovery and Climate Experiment (GRACE) mission (*8*) that is currently mapping Earth's gravity field. Each GRAIL spacecraft has a single science instrument, the Lunar Gravity Ranging System (LGRS), which measures the change in distance between the two co-orbiting spacecraft as they fly above the lunar surface. The spacecraft are perturbed by the gravitational attraction of topography and subsurface mass variations that can be isolated and subsequently analyzed. Doing so requires correcting for perturbations due to spacecraft maneuvers, and non-conservative forces such as solar radiation pressure and spacecraft outgassing, and relativistic effects**,** as discussed further in the SOM.

GRAIL launched successfully from Cape Canaveral Air Force Station on 10 September 2012, aboard a Delta-II 7290H. The twin spacecraft embarked on separate low-energy trajectories to the Moon via the EL-1 Lagrange point (*9*) and inserted into

lunar polar orbit on 31 December 2011, and 01 January 2012. After a total of 27 maneuvers (*10*) to lower and circularize the orbits to ~55-km mean altitude (fig. S1, S2) and to align the spacecraft to their ranging configuration, GRAIL executed its Primary mapping Mission (PM) from March 1, 2012, through May 30, 2012, transmitting to Earth 637 MB of science data corresponding to >99.99% of possible data that could be collected. During the PM the inter-spacecraft distance varied between 82 and 218 km (fig. S3) to provide different sensitivities to the short and longer wavelength components of the gravity field. As exemplified in fig. S4, the root mean square (RMS) range-rate residuals from the LGRS Ka-band ranging system during the PM were generally of order 0.02–0.05 μm s^{-1}, a factor of two to five better than the mission requirements.

These observations have been integrated into a spherical harmonic representation of the lunar gravitational field, which we denote model GL0420A. This model extends to degree and order 420, corresponding to a spatial block size of 13 km. Gravity field determination requires the application of numerous corrections, summarized in the SOM, and emphasis in the production of this model has been on resolving short-wavelength structure.

The global free-air gravity field of the Moon is shown in Fig. 1A, and the Bouguer gravity in Fig. 1B. The latter reveals the gravitational structure of the subsurface after subtraction of the attraction of surface topography from the free-air gravity. As with previous lunar gravity models, the GRAIL field shows the prominent mascons, the largest of which are associated with nearside basins, as well as the broad structure of the highlands. However, the much higher spatial resolution and greatly improved signal quality with respect to previous models combine to reveal distinctive gravitational

signatures of many features not previously resolved, including impact basin rings, central peaks of complex craters, volcanic landforms, and smaller simple, bowl-shaped craters.

Understanding the spectral content of the observations facilitates interpretation of the gravity maps. In Fig. 2A we compare the RMS free-air power and formal error spectra of GL0420A to previous models from the Lunar Prospector (LP150Q) and Kaguya (SGM150J) missions. As with other planetary potential field models, the RMS power of lunar gravity is greatest at low degrees (long wavelengths) and least at high degrees (short wavelengths). The empirical best-fit power law to the lunar gravity field is $2.5 \times 10^{-4}\, l^2$, where l is the spherical harmonic degree. The degree at which the error spectrum intersects the power spectrum represents traditionally the spatial scale at which the gravitational coefficients (*cf.* eqns. S1 and S2) are 100% in error. However, the error spectrum of model GL0420A does not intersect the model power, which indicates that still higher-resolution fields may ultimately be derived from GRAIL's PM data set. It is notable that GL0420 fits late-stage PM data (May 19-29) when the periapsis altitude was ~17-25 km, at 1 - 1.5 μm or 10-15 times the intrinsic quality of the Ka-band range rate observations. The gravitational power of LP and Kaguya are comparable and approximately match that of GRAIL to about degree 100 (block size 54 km), but the GRAIL errors at spatial scales associated with large to intermediate impact basins [degrees ≤ 60 (90 km)] are 3-5 orders of magnitude smaller than those of LP and Kaguya.

The coherence (see SOM) between gravity and the gravity predicted from unit-density topography for GRAIL, LP, and Kaguya are compared in Fig. 2B. Owing to its direct sampling of farside gravity, Kaguya displays a higher coherence than LP; the Kaguya correlation peaks at approximately degree 60 and falls off rapidly with increasing

degree due to an inability to sense the full gravitational power of smaller-scale mass variations. The LP data exhibits overly low global coherence at all degrees despite its lower mapping altitude (40-100 km) than Kaguya (100 km), though a recent re-analysis of LP (*11*) that focused on improving resolution where direct tracking is available shows a higher nearside coherence. In contrast, GL0420A reveals a very high correlation with topography to high degrees. The departure of the coherence spectra of LP and Kaguya from the GRAIL spectrum at degrees 30 and 60, respectively, indicate that despite approximately matching the power, these fields are significantly in error at higher degrees. Between degrees 80 (68 km) and 320 (17 km), 98.5% of the Moon's gravity signal is attributable to topography.

The magnitudes of short-wavelength Bouguer anomalies (Fig. 1B) are consistent with the high, but not perfect, coherence shown in Fig. 2B. Comparison of the maps shows that the range in Bouguer anomaly is typically up to ~10% that of the free-air gravity anomaly, which translates to a 1% ratio in terms of power. The lack of perfect correlation between gravity and topography is a result of lateral variations in crustal density and/or subsurface composition, such as due to the presence of magmatic plutons. Though this signal is small, the high-quality measurements ensure that it is easily resolvable (Fig. 2A) at a level that permits investigation of processes associated with impact cratering, such as brecciation, ejecta deposition and impact melting, as well as volcanic emplacement.

In general, gravity and topography should become more highly correlated with increasing degrees because the strength of the lithosphere is increasingly able to support topographic loads at shorter wavelengths without compensating masses at depth, and because the signals associated with subsurface anomalies are increasingly attenuated with

increasing degree. The high coherence exhibited by the Moon (Fig. 2C) is extraordinary and implies that the majority of the short-wavelength gravity signal is a result of surface topography, most of which is related to abundant impact craters. To retain a high coherence, the crust beneath those landforms must have been pervasively fractured and homogenized. Short-wavelength, lateral density variations due to magmatism, variable porosity, or regionally variable impact melting imparted during the early, post-accretional era of high impact flux are sparsely preserved at ~30–130 km scales. At harmonic degrees lower than about 60 (90 km), the coherence displays greater variability within the general pattern of a rapid decrease with decreasing degree. At these longer wavelengths the lower coherence reflects the heterogeneity of lunar interior structure: thinning of the crust beneath impact basins, large-scale variations in crustal composition indicated by orbital remote sensing (*12*), and lateral variations in mantle composition and possibly temperature, such as the variations associated with Procellarum KREEP terrain (*13, 14*). At the highest degrees (>330) the coherence falls off because of longitudinal gaps in the spacecraft ground tracks. As refined models are developed using data from GRAIL's extended mission with lower altitudes and closer cross-track spacing (*15, 16*), we anticipate that the high coherence will extend to even higher degrees than shown here.

As shown in Fig. 2C, the gravity–topography coherence exhibited by the Moon is unlike that observed for any other terrestrial planet. From degrees 25-200, Earth's coherence is variable, with an average value of ~0.7. The coherence spectrum reflects a contribution from the continents, whose gravity–topography relationships are dominated by crustal thickness variations and erosion, and include influences from compositional variability and tectonic and volcanic processes at shorter wavelengths. The Earth's ocean

basins also contribute to the correlation, but because in many places both gravity and seafloor bathymetry are estimated from satellite altimetry (*17*), the two data sets are not independent and therefore not straightforward to interpret in a geophysical sense. The coherence for Venus peaks at 0.9 at degree 3 and falls off rapidly. This falloff in coherence may reflect a combination of large-scale volcanic resurfacing (*18*) that smoothed the surface at short and intermediate length scales, the thick atmosphere, which screened small impacts, density anomalies related to mantle convection, and the orbital altitude of the Magellan spacecraft. The coherence for Mars is greatest at low degrees, at which it is governed by large-scale topography (*19*) such as the Tharsis province (*20*). Mercury's coherence does not exceed 0.6, but the spherical harmonic models of gravity (*21*) and topography (*22*) inadequately sample the southern hemisphere of the planet because of the eccentric orbit of the MESSENGER spacecraft. Our expectations are that at high degrees Mercury should display a coherence broadly similar to that of the Moon, because of its heavily cratered surface. The lithosphere of Mars is heavily cratered in the southern hemisphere, but in the northern hemisphere and on the Tharsis rise volcanic resurfacing extended well past the period of high impact flux. The extent to which the observed coherence of Mars reflects crustal structure as opposed to the quality of the data is not clear.

The free-air and Bouguer gravity anomaly maps in Fig. 1 show the distinctive character of the lunar gravity field. The free-air map shows rich short-wavelength structure and resolves virtually all craters on the Moon greater than 30 km in diameter and many less than 20 km in diameter. The highlands, because of the higher density of impact structures, show more gravitational detail at short wavelengths than the volcanic

plains of the maria. In comparison with the free-air gravity, the Bouguer map is smooth at short wavelengths because the contributions to free-air gravity from impact craters derive mostly from their topography. This characteristic of lunar structure facilitates the isolation of density variations within the crust (*23*). As noted in previous studies (*5, 24*), large impact basins are accompanied by thinning of the crust beneath the basin cavity, due to excavation and rebound associated with the impact and basin formation process (*25*). In some cases there is a second contribution from fill from mare volcanism subsequent to basin formation.

Regional comparisons of free-air gravity anomaly, topography (*26*), and Bouguer gravity anomaly reveal features that inform understanding of lunar structure and evolution. Fig. 3A shows an area of the farside highlands that includes the 417-km-diameter Korolev basin as well as many complex and simple craters. The maps also illustrate the ability of GRAIL to resolve Korolev's peak ring. In contrast to previous fields, GRAIL resolves Korolev's central Bouguer high to lie entirely within the central peak ring, and the annular low to reside on the crater floor and not beneath the walls. The observed gravitational structure implies that there is a density deficit under the floor either due to less dense, possibly brecciated, surface material filling the interior of Korolev restricted to outside the peak ring, or thickened crust produced by sub-isostatic depression of the mantle.

Fig. 3A also demonstrates the spatial manifestation of the Moon's high coherence: the free-air map resembles the topography map at intermediate to short length scales. In contrast, the Bouguer map is generally smooth; removal of the gravitational attraction of topography reveals that there is much less short-wavelength structure attributable to

subsurface density variations. Thinning of the crust beneath Korolev (*27*) represents the primary contribution to subsurface density variations in this area. The negative Bouguer signature of the rim of Doppler crater, just to the south of Korolev, may be indicative of brecciation.

A region in the western part of Oceanus Procellarum, shown in Fig. 3B, highlights the subsurface structure of maria and crust in this region. Positive Bouguer gravity anomalies in the maria are part of a pattern in western and southern Oceanus Procellarum (*cf*. Fig. 1B) that may indicate locally denser or thicker mare material. These Bouguer anomalies may help to define the boundary of either the Procellarum KREEP Terrane (*28*) or of the proposed Procellarum impact basin (*29*).

As exemplified by Fig. 3B, gravitational signatures of ghost craters in the maria are not abundant, indicating either that the density contrast between the maria and underlying crust is not great or that underlying crust has been reworked such that these structures have not been preserved. Both possibilities would be consistent with a scenario in which highland crust that underlies the maria has been significantly modified by dikes and intrusions (*30*).

Results from GRAIL's Primary Mission provide a new view of the lunar crust and bring quantitative geophysical description of the internal structure of the Moon into a spatial realm commensurate with the scales surface geological features. More broadly, the observed gravitational structure increases understanding of the role of impact bombardment on the crusts of terrestrial planetary bodies.

References and Notes

1. M. T. Zuber, D. E. Smith, D. H. Lehman, M. M. Watkins, paper presented at the Int. Astronaut. Congress, Naples, Italy, 2012.
2. P. M. Muller, W. L. Sjogren, Mascons: Lunar mass concentrations. *Science* **161**, 680 (1968).

3. N. Namiki *et al.*, Farside gravity field of the Moon from four-way Doppler measurements of SELENE (Kaguya). *Science* **323**, 900 (2009).
4. Materials and methods are available as supporting material on *Science Online*.
5. A. S. Konopliv *et al.*, Gravity field of the Moon from Lunar Prospector. *Science* **281**, 1476 (1998).
6. A. S. Konopliv, S. W. Asmar, E. Carranza, W. L. Sjogren, D.-N. Yuan, Recent gravity models as a result of the Lunar Prospector mission. *Icarus* **150**, 1 (2001).
7. E. Mazarico, F. G. Lemoine, S.-C. Han, D. E. Smith, GLGM-3, a degree-150 lunar gravity model fom the historical tracking data of NASA Moon orbiters. *J. Geophys. Res.* **115**, doi:10.1029/2009JE003472 (2010).
8. B. D. Tapley, S. Bettadpur, J. C. Ries, P. F. Thompson, M. M. Watkins, GRACE measurements of mass variability in the Earth system. *Science* **305**, doi: 10.1126/science.1099192 (2004).
9. R. B. Roncoli, K. K. Fujii, paper presented at the AIAA Guidance, Navigation and Control Conference, Toronto, Ontario, Canada, 2-5 August 2010 2010.
10. S. J. Hatch, R. B. Roncoli, T. H. Sweetser, paper presented at the AIAA Astrodynamics Conf., Toronto, CA, 2-5 August, 2010 2010.
11. S.-C. Han, E. Mazarico, D. D. Rowlands, F. G. Lemoine, S. Goossens, New analysis of Lunar Prospector radio tracking data brings the nearside gravity field of the Moon with an unprecedented resolution. *Icarus* **215**, 455 (2011).
12. M. Ohtake *et al.*, The global distribution of pure anorthosite on the Moon. *Nature* **461**, 236 (2009).
13. M. A. Wieczorek, R. J. Phillips, The Procellarum KREEP Terrane: Implications for mare volcanism and lunar evolution. *J. Geophys. Res.* **105**, 20 (2000).
14. C. K. Shearer *et al.*, Thermal and Magmatic Evolution of the Moon. *Rev. Mineral. Geochem.* **60**, 365 (2006).
15. M. T. Zuber, D. H. Lehman, D. E. Smith, T. L. Hoffman, S. W. Asmar, Gravity Recovery and Interior Laboratory (GRAIL): Mapping the lunar interior from crust to core. *Space Sci. Rev.*, (2012).
16. T. H. Sweetser, M. S. Wallace, S. J. Hatch, R. B. Roncoli, paper presented at the AIAA Astrodynamics Specialist Conference, Minneapolis, MN, 13-16 August 2012 2012.
17. D. T. Sandwell, W. H. F. Smith, Marine gravity anomaly from GEOSAT and ERS 1 satellite altimetry. *J. Geophys. Res.* **102**, 10 (1997).
18. R. J. Phillips *et al.*, Impact craters and Venus' resurfacing history. *J. Geophys. Res.* **97**, 15 (1992).
19. D. E. Smith *et al.*, Mars Orbiter Laser Altimeter: Experiment summary after the first year of global mapping of Mars. *J. Geophys. Res.* **106**, 23689 (2001).
20. M. T. Zuber *et al.*, Internal structure and early thermal evolution of Mars from Mars Global Surveyor topography and gravity. *Science* **287**, 1788 (2000).
21. D. E. Smith *et al.*, Gravity field and internal structure of Mercury from MESSENGER. *Science* **335**, doi:10.1126/science.121880 (2012).
22. M. T. Zuber *et al.*, Topography of the northern hemisphere of Mercury from MESSENGER laser altimetry. *Science* **335**, doi:10.1126/science.1218805 (2012).
23. J. C. Andrews-Hanna, e. al., Giant dikes and the early expansion of the Moon revealed by GRAIL gravity gradiometry. *Science*, (2012).
24. M. T. Zuber, D. E. Smith, F. G. Lemoine, G. A. Neumann, The shape and internal structure of the Moon from the Clementine mission. *Science* **266**, 1839 (1994).
25. H. J. Melosh, *Impact Cratering: A Geologic Process*. (Oxford University Press, New York, 1989), pp. 245.
26. D. E. Smith *et al.*, Initial observations from the Lunar Orbiter Laser Altimeter (LOLA). *Geophys. Res. Lett.* **37**, doi:10.1029/2010GL043751 (2010).
27. M. A. Wieczorek *et al.*, The crust of the Moon as seen by GRAIL. *Science*, (2012).

28. B. L. Jolliff, J. J. Gillis, L. Haskin, R. L. Korotev, M. A. Wieczorek, Major lunar crustal terranes: Surface expressions and crust-mantle origins. *J. Geophys. Res.* **105**, 4197 (2000).
29. P. H. Cadogan, Oldest and largest lunar basin? *Nature* **250**, 315 (1974).
30. J. W. Head, L. Wilson, Lunar mare volcanism: Stratigraphy, eruption conditions and the evolution of secondary crusts. *Geochim. Cosmochim. Acta* **56**, 2155 (1992).
31. T. D. Moyer, "Formulation for Observed and Computed Values of Deep Space. Network Data Types for Navigation", doi: 10.1002/0471728470.fmatter (John Wiley & Sons, Hoboken, NJ, 2005).
32. D. E. Pavlis, S. G. Poulouse, J. J. McCarthy, "GEODYN Operations Manuals" (SGT, Inc., Greenbelt, MD, 2009).
33. R. E. Ulman, "SOLVE Program: Mathematical Formulation and Guide to User Input" *Constract NAS5-31760* (Hughes/STX Contractor Report, 1994).
34. F. G. Lemoine, D. E. Smith, M. T. Zuber, G. A. Neumann, in *Global Gravity Field and Its Temporal Variations,* R. Rapp, A. Cazenave, R. Nerem, Eds. (Springer-Verlag, Berlin, 1996), IAG Symposium, held during the XXI General Assembly of the Int. Union of Geodesy and Geophysics, pp. 176-185.
35. E. Mazarico *et al.*, Orbit determination of the Lunar Reconnaissance Orbiter. *J. Geod.* **86**, 193 (2012).
36. S. B. Luthcke *et al.*, Monthly spherical harmonic gravity field solutions determined from GRACE inter-satellite range-rate data alons. *Geophys. Res. Lett.* **33**, doi: 10.10292/005GL024846 (2006).
37. J. A. Marshall, S. B. Luthcke, Modeling radiation forces acting on TOPEX/Poseidon for precision orbit determination. *J. Spacecraft Rockets* **31**, 99 (1994).
38. R. S. Park *et al.*, Gravity Recovery and Interior Laboratory simulations of static and temporal gravity field. *J. Spacecraft Rockets* **49**, 390 (2012).
39. W. M. Kaula, *Theory of Satellite Geodesy*. (Blaisdell, Waltham, 1966), pp. 124.
40. M. A. Wieczorek, Gravity and topography of the terrestrial planets. *Treatise on Geophysics* **10**, 165 (2007).
41. J. G. Williams, A scheme for lunar inner core detection. *Geophys. Res. Lett.* **34**, doi:10.1029/2006GL028185 (2007).
42. M. A. Wieczorek, R. J. Phillips, Potential anomalies on a sphere: Applications to the thickness of the lunar crust. *J. Geophys. Res.* **103**, 1715 (1998).
43. D. D. Rowlands, R. D. Ray, D. S. Chinn, F. G. Lemoine, Short-arc analysis of intersatellite tracking data in a gravity mapping mission. *J. Geod.* **76**, 307 (2002).
44. H. Goiginger *et al.*, paper presented at the General Assembly of the European Geosciences Union, Vienna, Austria, 4-8 April 2011 2011.
45. A. S. Konopliv, W. B. Banerdt, W. L. Sjogren, Venus gravity: 180th degree and order model. *Icarus* **139**, doi:10.1006/Icar.1999.6086 (1999).
46. A. S. Konopliv *et al.*, Mars high resolution gravity fields from MRO, Mars seasonal gravity, and other dynamical parameters. *Icarus* **111**, 401 (2011).
47. D. E. Smith *et al.*, The Lunar Orbiter Laser Altimeter investigation on the Lunar Reconnaissance Orbiter mission. *Space Sci. Rev.* **150**, 209 (2010).

The GRAIL mission is supported by NASA's Discovery Program and is performed under contract to the Massachusetts Institute of Technology and the Jet Propulsion Laboratory. We are grateful to the GRAIL spacecraft, instrument and operations teams for outstanding support. We thank J. Andrews-Hanna, J. Head, W. Kiefer, P. McGovern, F. Nimmo J. Soderblom and M. Sori for helpful comments on the manuscript. The data used in this study will have been archived in the Geosciences Node of the NASA Planetary Data System by the time of publication.

12 October 2012

Figure Legends

Fig. 1. (**A**) Free-air and (**B**) Bouguer gravity anomaly maps from GRAIL lunar gravity model GL0420A, to spherical harmonic degree and order 420. Maps are in Molleweide projection centered on 270°E longitude and show the nearside on the right and farside on the left. Gravity is plotted in units of milliGalileos, where 1000 mGal = 1 cm s^{-2}. A crustal density of 2560 kg m^{-3} was assumed in the Bouguer correction. In the Bouguer map degrees < 6 have been filtered out to highlight mid- to short-wavelength structure. Further details regarding the Bouguer map are found in the SOM.

Fig. 2. (A) RMS power and **(B)** coherence versus degree for the gravity fields determined by GRAIL, Kaguya, and Lunar Prospector. **(C)** Coherence between gravity and topography versus degree of the Moon in comparison with other terrestrial planets. In **(B)** all gravity models are compared with topography from the Lunar Orbiter Laser Altimeter (*26*). Data sets used in **(C)** are given in Table S1.

Fig, 3. (A, B) From top to bottom, Mercator projections of free-air gravity, topography, and Bouguer gravity. Frames in **(A)** highlight the area surrounding the Korolev impact basin, at center. Frames in **(B)** show the western limb of Oceanus Procellarum. Details of free-air and Bouguer gravity are the same as in Fig. 1. Topography is from a LOLA 1/64^{o} grid.

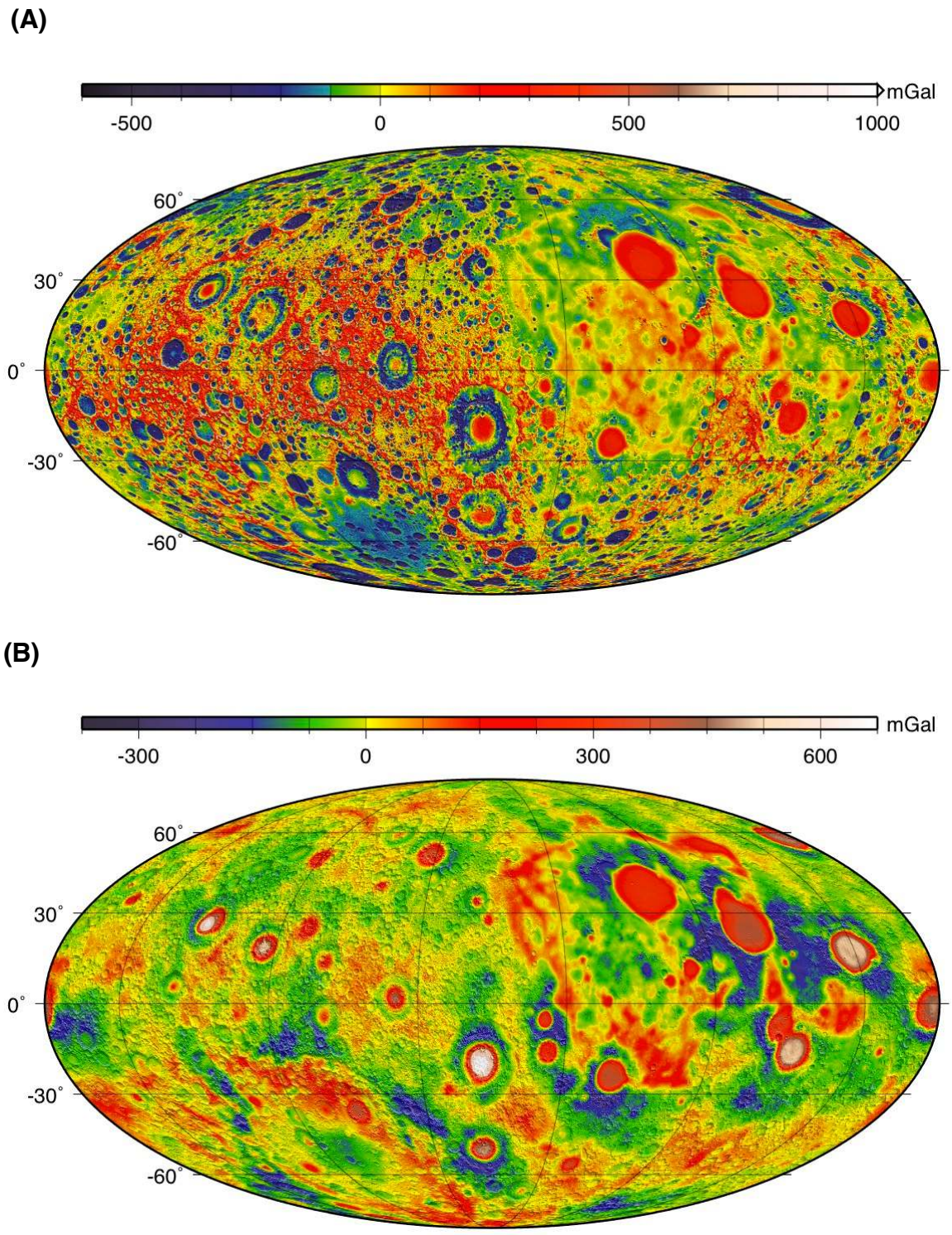

Figure 1
Zuber et al.

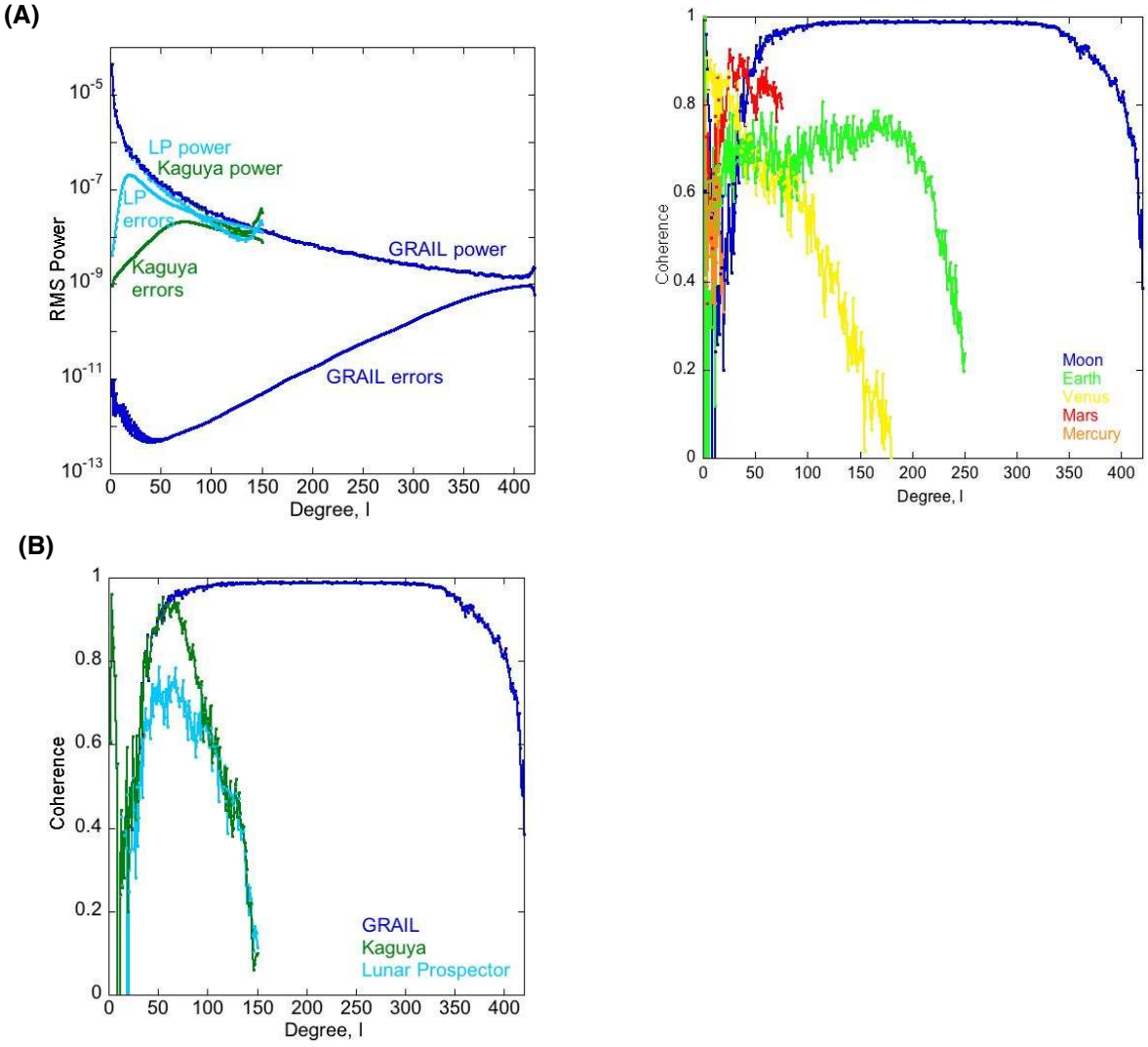

Figure 2
Zuber et al.

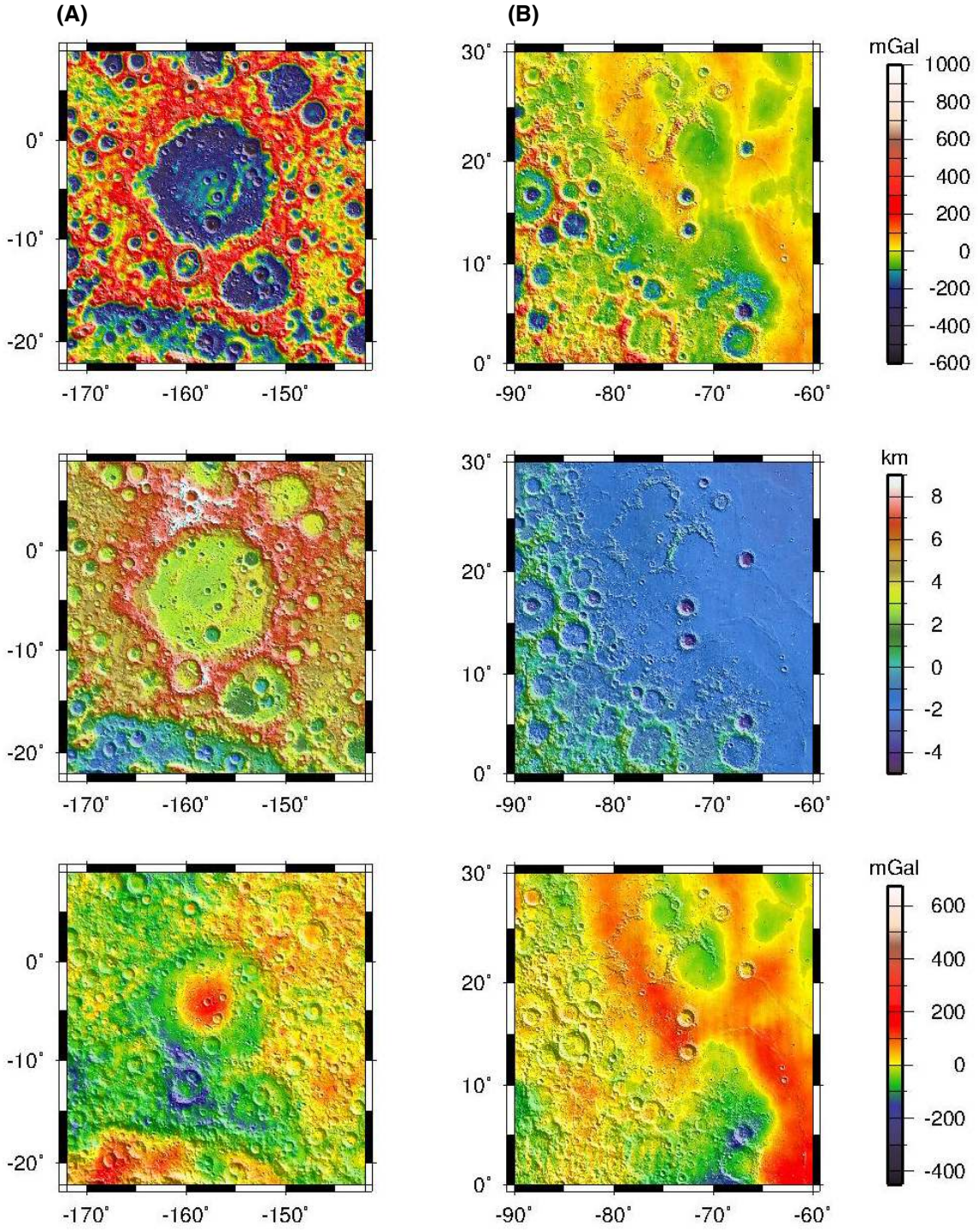

Figure 3
Zuber et al.

Supporting Online Material

Mapping Orbit

During the Primary Mission (PM) the dual GRAIL spacecraft, Ebb and Flow, co-orbited the Moon at an inclination of 89.9^{o} and at an average altitude of 55 km. However, in practice the orbit deviated from circular due to perturbations by the lunar gravity field. Fig. S1 shows the minimum altitude at which measurements were obtained over the course of the PM, and fig. S2 shows the periapsis and apoapsis of the spacecraft over the course of the PM. Note that because of the ellipticity of the orbit, particularly in the early and late stages of mapping, much of the lunar mid-latitudes were mapped from altitudes of 30 km or less, and in these areas gravity is resolved at finer spatial scales than in the polar regions. Fig. S3 shows the separation and drift rate of the spacecraft over the course of the PM. Note that although 27 maneuvers were required to achieve the mapping orbit, only one maneuver was executed during the PM, and this was to adjust the drift rate of the spacecraft to avoid multipath and spacecraft-to-spacecraft visibility issues. Over the course of the PM, the distance between the two spacecraft was designed to vary from 82 to 218 km, which provided sensitivity to mass variations over different depths, and which allowed certain errors in the gravity model to be de-correlated.

Data Processing and Gravity Field Solution

In order to verify the complex analysis required in precision orbit determination and gravity field development, we developed independent gravitational field solutions using software analysis packages developed independently at the Jet Propulsion Laboratory and the Goddard Spaceflight Center. Solution GL0420A presented herein was developed at JPL, but it compares well with solutions of similar resolution developed with the same data at Goddard. The primary JPL software tool utilized in the production of GL0420A was MIRAGE (Multiple Interferometric Ranging and GPS Ensemble), a version of the JPL Orbit Determination Program (ODP) (*31*) that has been optimized for planetary gravity fields. Of relevance to the current analysis, MIRAGE was used in precision orbit determination and gravity field development for the Lunar Prospector (*5, 6*) and Gravity Recovery and Climate Experiment (GRACE) (*8*) missions. Processing at the Goddard Space Flight Center utilized the GEODYN/SOLVE system of orbit analysis programs (*32, 33*), a version of which has also been optimized for planetary gravity field modeling. GEODYN/SOLVE has been used for precision orbit determination and gravity field modeling for the Clementine (*24, 34*), Lunar Prospector (*7*) and Lunar Reconnaissance Orbiter (*35*) missions as well as the GRACE mission (*36*).

When in view of Earth, the GRAIL spacecraft are periodically tracked from NASA's Deep Space Network in order to determine their absolute positions. Precise positioning is required so that spacecraft orbital position can be tied to the planet. Information about the lunar gravity field comes from the inter-spacecraft range-rate measurements from GRAIL's Lunar Gravity Ranging System. Each GRAIL spacecraft both transmits and receives Ka-band signals that measure the change in distance between the spacecraft, as well as S-band signals that align time tags. While ranging, GRAIL measures the change in spacecraft separation at a rate of 10 Hz, though in the current study we analyzed observations at a 5-Hz rate (corresponding to a sample approximately every 340 m along

the spacecraft ground track). Ka-band residuals during a typical day of mapping during the PM are shown in fig. S4. The root mean square (RMS) variation of the residuals is 0.05 m s^{-1}, which is approximately a factor of four better than GRAIL's range-rate requirement. We analyzed within MIRAGE, in a manner similar to that in previous solutions (*6*), the collective set of range-rate observations along with their times and locations. The resulting set of normal equations was inverted to produce a model of the gravitational field.

In determining precision orbits and in developing the gravitational field, we accounted for solar radiation pressure, the radiation pressure induced by the reflected solar and thermal radiation from the Moon, and third-body gravity perturbations from the Earth, Sun, and other planets. In addition we implemented relativistic corrections including light-time effects in the measurement model, and the modification of the equation of spacecraft motion that adjusts both the barycentric velocity and the Newtonian point mass acceleration of the Moon. We corrected the tracking data for DSN station coordinate effects, including Earth's polar motion, solid-Earth tides, and ocean loading. At the tracking stations we utilized meteorological data to correct the radiometric tracking data for propagation effects through Earth's troposphere.

The modeling included box-wing representation of the GRAIL orbiters that approximates the spacecraft as a series of flat plates with specific cross-sectional areas and specular and diffuse reflectivities. We oriented plates in space by means of the spacecraft attitude data, or quaternions (*37*).

In order to develop confidence that GRAIL's performance would be adequate to meet its measurement requirements, we performed, prior to lunch, an extensive set of simulations that took into account orbit geometry and the expected tracking schedule, spacecraft and instrument design and performance, and all known noise and error sources (*38*).

From the assembled orbital arcs we produced a spherical harmonic solution for the gravity field. We represent the gravitational potential, U, as a spherical harmonic expansion with normalized coefficients ($\bar{C}_{nm}$, $\bar{S}_{nm}$), expressed as (*39*)

$$U = \frac{GM}{r} + \frac{GM}{r}\sum_{l=2}^{\infty}\sum_{m=0}^{l}\left(\frac{R_M}{r}\right)^l \bar{P}_{lm}(\sin\varphi)\left[\bar{C}_{lm}\cos(m\lambda) + \bar{S}_{lm}\sin(m\lambda)\right] \qquad \text{(S1)}$$

where GM is the product of the gravitational constant and the Moon's mass, r is the body-fixed coordinate of radial distance, l and m are the spherical harmonic degree and order, $\bar{P}_{nm}$ are geodesy-normalized associated Legendre functions *cf.* (*40*), R_M is the lunar reference radius of 1737.4 km (*26*), and ϕ and λ are selenocentric latitude and longitude. The normalized (designated with overbar) and unnormalized gravitational coefficients are related by (*32*)

$$\begin{pmatrix} \bar{C}_{lm} \\ \bar{S}_{lm} \end{pmatrix} = \left[\frac{(l+m)!}{(l-m)!(2l+1)(2-\delta_{0m})}\right]^{1/2} \begin{pmatrix} C_{lm} \\ S_{lm} \end{pmatrix}. \qquad \text{(S2)}$$

The coefficients contain the information about the variation of gravity, and *l* and *m* describe the resolution of the field, which in practice is dictated by coverage and spacecraft altitude. In this representation low degrees and orders correspond to long wavelengths, and high degrees and orders correspond to short wavelengths.

Following the notation of (*40*) the power spectrum of the function *f* i*s*

$$S_{ff}(l) = \sum_{m=-l}^{l} f_{lm}^2 \quad . \tag{S3}$$

In Fig. 2a the observed RMS of the power follows the empirical relation $2.5 \times 10^{-4}\, l^2$, referred to as Kaula's Law (*39*). In the inversion to solve for the coefficients in equation (S2), this constraint is applied to the covariance matrix above degree and order 330 in order to resolve the highest-resolution structure in the model. However, we also developed solutions without a Kaula constraint and produced models that were reliable to approximately degree and order 350. Both constrained and unconstrained solutions will be archived in the NASA Planetary Data System according to the GRAIL Archiving Plan approved by NASA.

Comparison of the power spectra in Fig. 2a shows that model GL0420A represents an improvement over previous lunar gravity models at all degrees and orders. However, further improvements will be possible from additional corrections related to system performance (particularly timing) and more detailed modeling of non-conservative forces. In particular, additional corrections for solar radiation pressure will be especially important to reduce errors in long-wavelength terms that are relevant to the structure of the deep interior (*41*).

Gravity–Topography Coherence for the Terrestrial Planets

The coherence between gravity and the gravity predicted from unit density topography was calculated from the data sources in Table S1. Coherence is defined as

$$\gamma(l) = \left[\frac{S_{hg}(l)}{\left[S_{hh}(l) S_{gg}(l) \right]^{1/2}} \right]^2 , \tag{S4}$$

where the subscripts *g* and *h* correspond to gravity and topography, respectively. Since the gravitational signal at high degrees is non-linear in topography (*42*), especially for the Moon given the rugged surface relief associated with impact craters, calculation of the coherence using topography alone would give rise to lower values. To accurately calculate the gravity signal for degrees and orders up to 420, with a relative precision better than 10^{-4}, terms up to N=7 in the Taylor expansion (*42*) are employed.

In order to facilitate comparison, topography and gravity for terrestrial planets considered use only satellite observations, in the form of tracking data, gradiometry or altimetry to obtain solutions for gravity and altimetry.

Bouguer Gravity

In order to map subsurface density variations, we subtract the gravitational attraction

of surface topography to yield Bouguer gravity, assuming a density of 2560 kg m^{-3}. To isolate structures of interest, we removed the longest-wavelength signal by subtracting degrees<6 in Fig. 1B and the Bouguer maps in Fig. 3. Simulations of gravitational field recovery via satellite-to-satellite tracking performed in support of the GRACE mission (*43*) document that for a high-inclination orbit, low-order coefficients are recovered remarkably well while higher order terms, particularly sectorals, are recovered less accurately. This result is borne out by the GL0420A field, as demonstrated in fig. S5. The figure shows the Bouguer anomaly coefficient amplitude vs. degree and order, from the GRAIL0420A gravity field and LOLA topography (cf. Table S1). Coefficients outside the region enclosed by dashed lines at degree 384 and order 324 contain much of the noise power in the solution and are consequently eliminated in Fig. 1B and the Bouguer maps in Fig. 3. The color scale gives the amplitude corresponding to normalized coefficients in Fig. 1B and is saturated above 10^{-8}.

Table S1. Data sets used in coherence calculation.

Planet	Data Type	Model	Resolution, degree and order#	Reference	Comment
Moon	Gravity	GL0420A	420x420		This study
	Topography	MoonTopo1439	1439x1439	*	Spherical harmonic expansion of LOLA topography (*26*)
Earth	Gravity	GOCO02S	250x250	(*44*)	Satellite-only field including GOCE, GRACE, Champ, SLR
	Topography	SRTMP2160	2160x2160	*	SRTM (continents) + bathymetry (oceans)
Venus	Gravity	VENUS180U	180x180	(*45*)	Magellan gravity
	Topography		719x719	*	Magellan altimetry
Mars	Gravity	MRO110C	110x110	(*46*)	MRO gravity
	Topography	MarsTopo719	719x719	(*19*)	Spherical harmonic expansion of MOLA topography (*19*)
Mercury	Gravity	HgM003	20x20	Updated from (*21*)	MESSENGER gravity
	Topography	MLA	20x20	(*22*)	MESSENGER altimetry

*http://www.ipgp.fr/~wieczor/SH/SH.html

#Coherence was calculated to the lower resolution of gravity or topography.

FIGURES AND FIGURE CAPTIONS

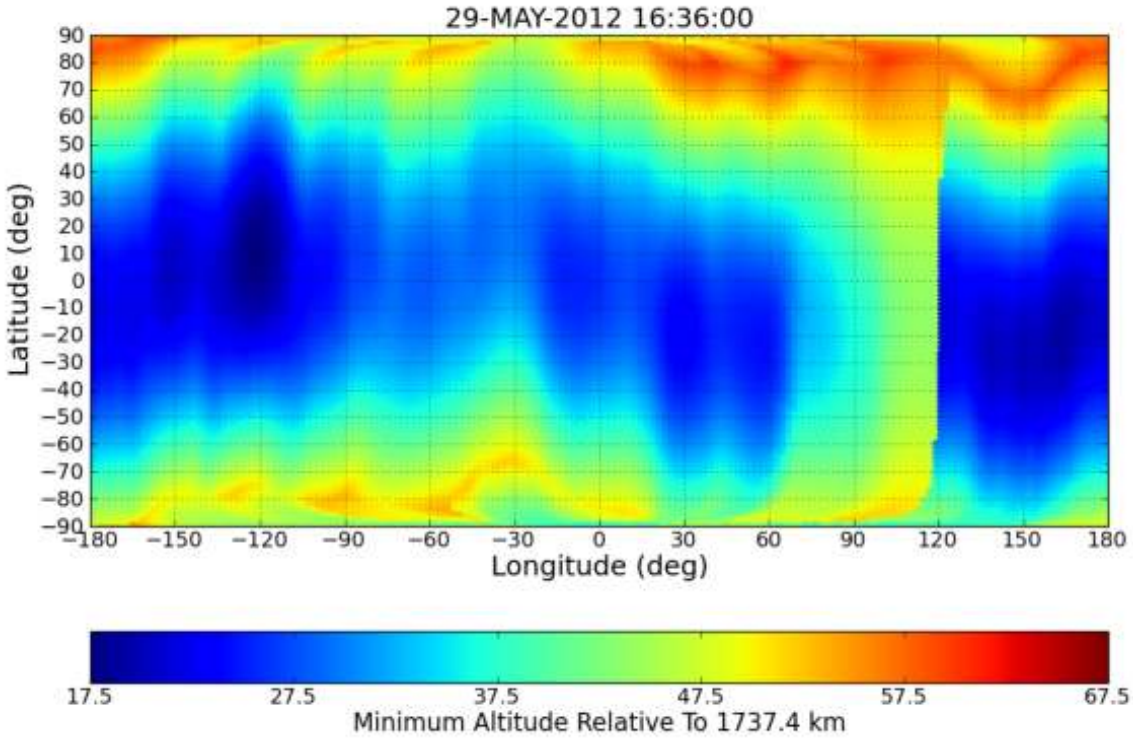

Figure S1. Variation of minimum altitude of the GRAIL spacecraft during the PM (1 March 2012 through 29 May 2012). Altitudes are relative the lunar mean radius of 1737.4 km (*26*) as measured by the Lunar Orbiter Laser Altimeter (*47*).

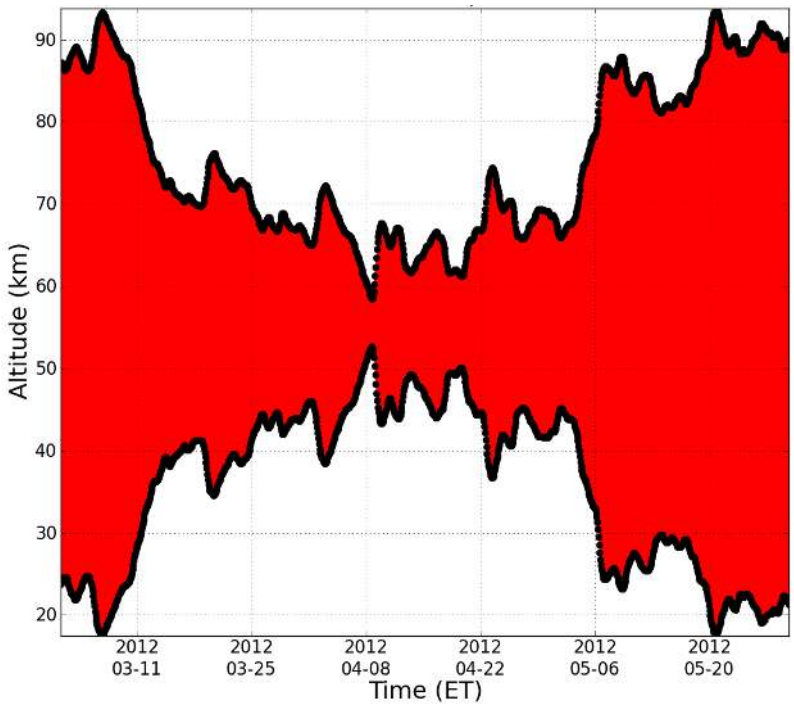

Figure S2. Orbital periapsis and apoapsis during GRAIL's PM. Altitudes are relative to the lunar mean radius of 1737.4 km (*26*) as measured by the Lunar Orbiter Laser Altimeter (*47*).

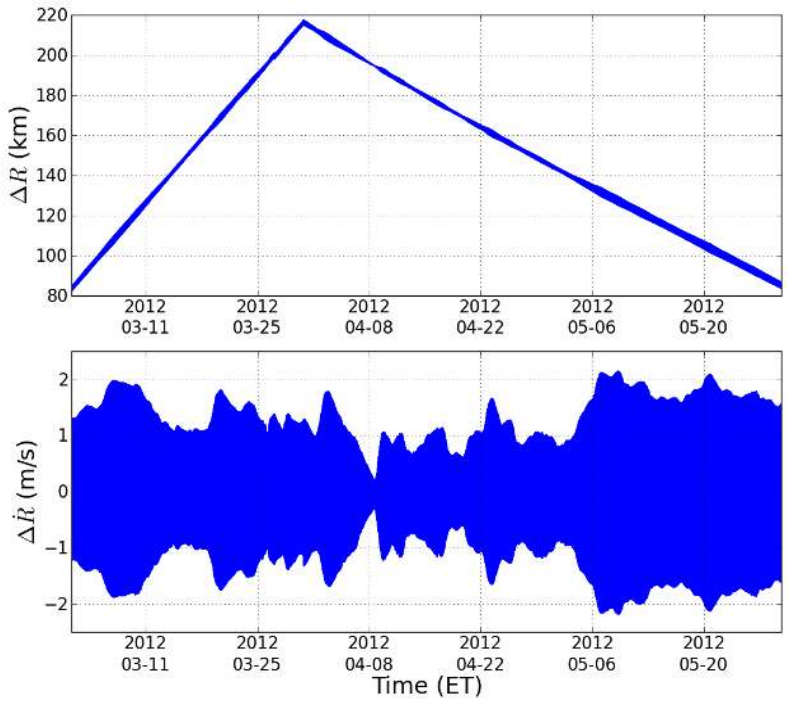

Figure S3. Spacecraft separation distance (ΔR ; top) and drift rate ($\Delta \dot{R}$; bottom) of the GRAIL spacecraft during the PM.

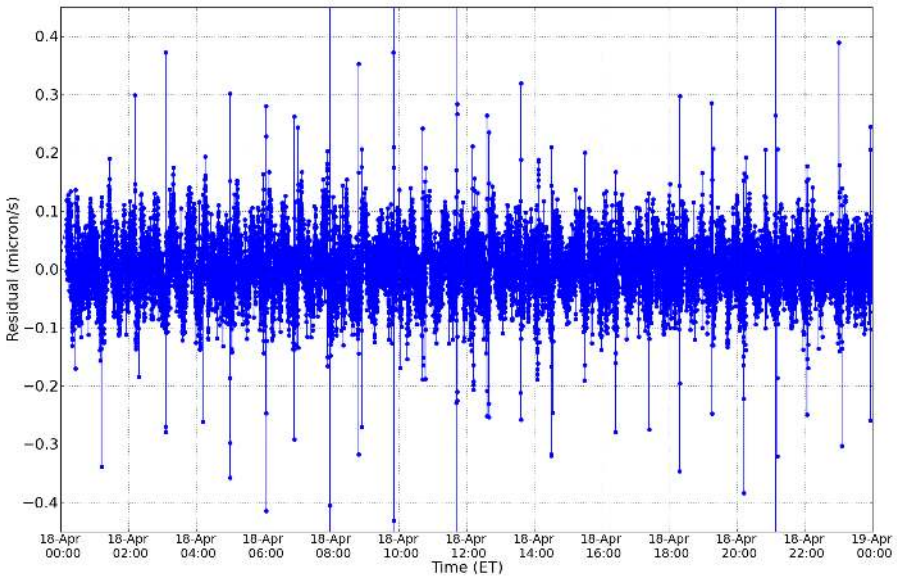

Figure S4. Ka-band range rate residuals during a typical day during the PM.

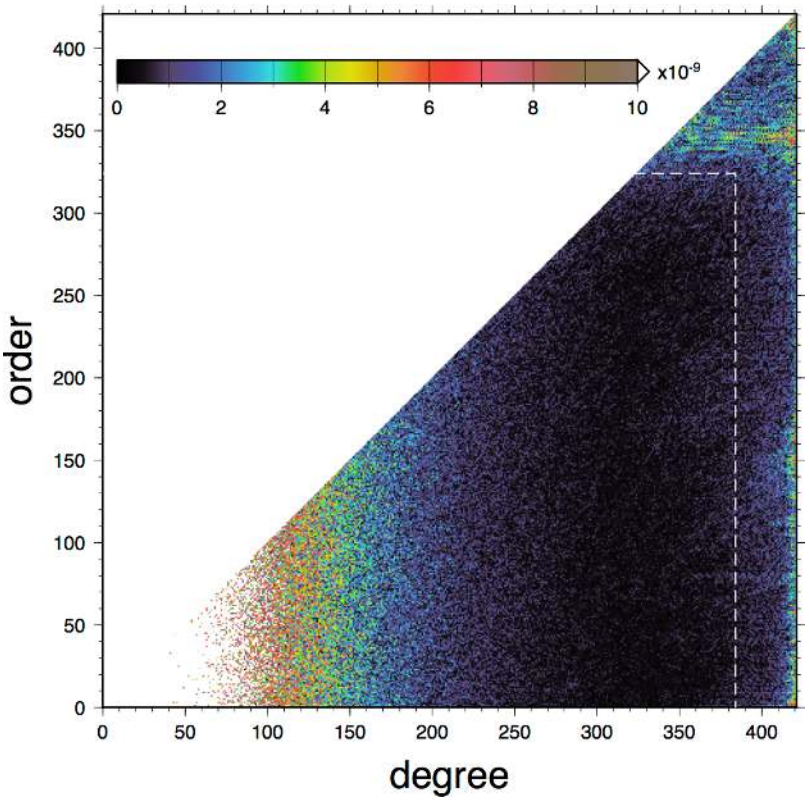

Figure S5. GRAIL gravity model GL0420A coefficient amplitudes plotted as degree vs. order. Low degrees and orders show the most power in the system. At degrees above 384 and orders above 324 the higher power is due to noise and are removed.